Materials Today Communications 39 (2024) 109192

Contents lists available at ScienceDirect

Materials Today Communications

journal homepage: www.elsevier.com/locate/mtcomm

Advanced microstructural characterization in high-strength steels via machine learning-enhanced high-speed nanoindentation and EBSD mapping

Federico Bruno [a,b], Georgios Konstantoupoulos [c], Edoardo Rossi [d,*], Gianluca Fiore [a], Costas Charitidis [c], Marco Sebastiani [d], Luca Belforte [b], Mauro Palumbo [a]

[a] Department of Chemistry, University of Turin, Via Pietro Giuria 7, Torino 10125, Italy
[b] Materials Engineering and Sustainability, Centro Ricerche Fiat, C.R.F. S.C.p.A., Corso Settembrini 40, Torino 10135, Italy
[c] RNANO Lab.—Research Unit of Advanced, Composite, Nano-Materials & Nanotechnology, School of Chemical Engineering, National Technical University of Athens, Athens, Zographos GR-15773, Greece
[d] Department of Civil, Computer Science and Aeronautical Technologies Engineering, Roma Tre University, Via della Vasca Navale 79, Rome 00146, Italy

ARTICLE INFO

Keywords:
Advanced High-Strength Steels
High-speed nanoindentation
EBSD
Machine learning

ABSTRACT

This research investigates the nanoscopic features of Advanced High-Strength Steels (AHSS) through a bottom-up approach employing high-speed nanoindentation mapping (HSNM) to elucidate structure-property relationships. The influence of grain boundaries on nanomechanical properties was documented, highlighting the challenge of SEM-EBSD analysis in differentiating phases with identical crystal structures (BCC, FCC, etc.). Integrating SEM-EBSD with HSNM in the same region of interest is essential for detailed insights into phase/microstructure distribution and accurate grain boundary identification. A modular four-step analysis protocol, designed and validated on ferritic-bainitic TRIP steels (TBF), leverages machine learning-enhanced HSNM for significant advancements in AHSS design. The initial phase involves the application of the expectation-maximization algorithm for probability distribution fitting of HSNM data, deriving primary mechanical phase statistics. This exclusively facilitates the correlation of elastic modulus and hardness for each phase/microstructure using nanoindentation data. Further refinement of phase/microstructure to mechanical property correlations was achieved through a supervised machine learning approach, ensuring precise association between EBSD and nanoindentation data. This includes detailed image analysis and clustering of nanoindentation data, enhancing the precision in phase recognition. This methodology addresses the critical challenges in developing 3rd Generation AHSS, aiming to fill the gap in accurately identifying and quantifying phases such as martensite, austenite, bainite, and ferrite, thereby reducing classification and measurement uncertainties. The approach contributes to the fundamental understanding of AHSS microstructures and provides a scalable framework for the comprehensive characterization of structural materials.

1. Introduction

TRIP (Transformation Induced Plasticity) steels belong to the category of Advanced High-Strength Steels (AHSS). Their microstructure is characterized by a ferrite matrix interspersed with varying proportions of retained austenite, martensite, and bainite. The production of TRIP steels involves an isothermal process at an intermediate temperature, leading to bainite formation [1]. This specific thermal treatment is termed "austempering." Bainite and ferrite predominance increases with higher silicon and aluminum contents. Conversely, the presence of martensite (unstable at room temperature) is reduced, while an increase in silicon and carbon content in the steel stabilizes the retained austenite, increasing its quantity [1].

In terms of mechanical performance, TRIP steels surpass many others. A notable feature is the transformation of retained austenite into martensite under mechanical strain [1]. This transformation is influenced by the carbon content, which affects the chemical impetus for the conversion, the inherent transformation strain, and the flow characteristics of the retained austenite. Dimatteo et al. [2] noted that an optimal carbon content (ranging between $> 0.5-0.6\%$ and $< 1.8\%$) enhances

* Corresponding author.
E-mail address: edoardo.rossi@uniroma3.it (E. Rossi).

https://doi.org/10.1016/j.mtcomm.2024.109192
Received 13 March 2024; Received in revised form 1 May 2024; Accepted 10 May 2024
Available online 14 May 2024

the TRIP effect, subsequently improving elongation [2,3]. With lower carbon content, austenite transforms almost instantly upon deformation, elevating the work hardening rate and formability during processes like stamping. Conversely, the retained austenite remains stable with higher carbon content, transforming only under strains exceeding typical forming levels. In such cases, the austenite converts to martensite during subsequent deformations, such as impacts. The dispersion of harder secondary phases within the softer ferrite matrix results in a significant work hardening rate, similar to what is observed in dual-phase (DP) steels [1]. In the automotive industry, TRIP steels are favored for their lightweight properties and are commonly used in Body in White (BIW) components, including cross and side members [1]. However, the intricate microstructure of TRIP steels, which underpins their exceptional macroscopic mechanical attributes, poses challenges for accurate characterization using conventional metallographic techniques.

Therefore, understanding TRIP steels' microstructure, properties, and phases is paramount [4]. In recent decades, innovative characterization methods, including nanoindentation, have revolutionized the study of materials with intricate microstructures that influence mechanical properties. Nanoindentation has emerged as a preferred technique for measuring material hardness at the nanoscale, offering insights into microstructures and their stress-induced transformations. Typical data analysis involves the Oliver W. and Pharr G. method [5], which, since 1992, has been the gold standard used to evaluate the nano-properties of materials [6–12]. Moreover, nanoindentation is a critical technique for assessing downcycling phenomena from a circular economy perspective, as described by Capricho [9].

Regarding steels nanomechanical properties, it has been shown that their nano-hardness values depend on two factors: (i) phases and microstructure originated by thermal treatments [13] and (ii) the orientation of the grains [14], changing according to the orientation of each type of phase/microstructure and its volume fraction. In the literature, the study of the phase/microstructure (P/M) relationships in steels and the assessment of their properties with nanoindentation is quite popular. Notably, efforts have been extensively focused on distinguishing P/M relationships of ferritic-bainitic TRIP steels and studying their mechanical properties, including transformation-induced hardening, which is paramount to understanding potential failure initiation, whether mechanical or chemical [15–20].

However, a significant drawback in applying nanoindentation existed until recent technological developments. Indeed, classical grid nanoindentation provides (i) extremely localized, (ii) statistically limited, and (iii) time-consuming data [21,22]. However, recently, high-speed nanoindentation mapping (HSNM) [23], a cutting-edge technique, allowed for rapid mechanical property mapping over large areas with sub-micron-scale resolution. This method provides comprehensive datasets quickly, performing each nanoindentation and movement to the next location in less than one second, ultimately capturing the material response over vast areas with thousands of measurement points on average. Such advancements have been instrumental in correlating mechanical contrasts with phase contrasts, offering a deeper understanding of material behavior [24,25].

Complementing nanoindentation, SEM-EBSD provides in-depth phase identification, distribution mapping, grain boundary characterization, texture analysis (degree of crystallographic preferred orientation), and local strain variation analysis [8,26–35]. EBSD could be a valid method to perform as paired with SEM-EDS. It offers a holistic view of inclusions and their crystallographic features. However, a significant challenge remains: traditional EBSD analyses struggle to distinguish between phases like ferrite, martensite, bainite, and pearlite, even with machine learning.

As several studies demonstrate, coupling HSNM and EBSD represents a promising mean for P/M recognition [8,26–29]. This study proposes a multi-faceted analysis protocol, employing ML clustering on both images and high-speed nanoindentation data [36], to overcome most of the HSNM and EBSD coupling challenges for AHSS within the same Region of Interest (ROI) and shed light on structure-property relationships twofold.

A curated combined dataset was produced to train machine learning models and predict the uncorrelated instances between the two methods. In contrast, grain boundary detection supported the analysis to detect the pure response owed to each microstructure. When nanoindentation occurs along grain boundaries, the indented area will intercept more grains belonging to different phases/microstructures. Consequently, hardness and elastic modulus related to this measurement do not represent any phases/microstructures. So, all outcomes affected by the grain boundaries effect will be allocated as Grain Boundaries properties.

The outcomes of the proposed methodology give complete spatial information on the distribution of phases within the identified ROI, transformation-induced changes after nanoindentation experiments, and, most notably for their design, the relative content of retained austenite. Moreover, the authors provide a series of testing strategies, applicability ranges, and a general methodology to couple multiple observations from different techniques at the nanoscale, capable of being applied to more general phase/microstructure/properties identification problems in materials science in a modular and scalable strategy. Finally, validated characterization data outputs and transfer learning of such trained models can pave the way for acceleration in materials research of the 3rd generation AHSSs.

2. Materials and methods

2.1. Materials

TBF-1180 steel, a specific grade of TRIP steel, was analyzed for its chemical composition (Table 1). A plate of 3×3 cm was cut to perform chemical composition analysis employing a Quantometer (Thermo-Scientific ARL 3460 OES) using the normative ASTM E415–21 standard [37].

2.2. Methods

To preliminary observe the alloy microstructure, a sample, hot-mounted in non-conductive-polyphenolic-resin (curing temperature 180°C, heating time 3 min, cooling time 1 min; pressure 200 bar) and mechanically polished using standard sandpapers, was etched with fresh Klemm I solution, and the corroded surface was observed by using the Zeiss Observer Z1m Optical Microscope.

SEM-EBSD analysis (SEM Tescan FESEM 9000: 20 kV; 1 nA; EBSD Symmetry S2 Oxford Instruments; AztecCrystal provides data) was performed on an ad-hoc prepared TBF-1180 sample before nanoindentation to avoid observing strain-induced crystal lattice changes in the structural mapping. The sample was cold-mounted in conductive resin and mechanically polished using standard sandpapers down to a final step involving 40 nm colloidal silica [38]. The same sample was used also for nanoindentation testing. Before EBSD analysis, carbon tape was placed around the sample surface, and mounting resin was used to improve the sample's conductibility, hence the EBSP (electron backscatter diffraction pattern) resolution. The commercial "Re-classify" tool (AztecCrystal, Oxford Instruments) was used to perform the microstructure annotation in the EBSD map. This tool requires the user to create a featured map in which all the parameters chosen are used to implement a built-in machine-learning model. Once the map is made, the user assigns specific areas or points to the appropriate phase and microstructure based on visual map analysis. Each pixel will contain the

Table 1
Elemental analysis of TBF-1180.

C	Mn	P	S	Si	Al	Ti+Nb+V	Cr+Mo
0.2	2.53	0.0088	0.0005	1.45	0.056	0.005	0.107

values of the various features under consideration, which will then be used by the software algorithm to complete the map in real-time. However, an inherent challenge with this approach is the potential for user bias. Subjective decisions during the examination can vary among users, leading to discrepancies in the resulting maps. Despite this drawback, the tool's primary advantage lies in its ability to generate maps considering structures that cannot be recognized directly by the Kikuchi pattern. For this capability to be fully realized, the image must be high-resolution, and the phases/microstructures should be visually discernible.

2.3. High-speed nanoindentation mapping

Nanoindentation testing was conducted to identify the mechanical phase distribution in the TBF-1180 steel, complemented by EBSD mapping to provide a comprehensive understanding of the material's microstructure.

The mechanical mapping experiments employed the G200 nanoindenter (KLA Corp.) equipped with a Berkovich tip (E = 1141 GPa; ν = 0.07). Before high-speed nanoindentation mapping, the load-depth response and the properties were examined via Continuous Stiffness Measurement (CSM) [5], also offering a preliminary point-to-point correlation with EBSD and, most importantly, acted as a calibration for the subsequent high-throughput, high-speed mapping using the Express Test protocol, retrieving the average load required to achieve a 150 nm penetration depth on the softer phase. This step, therefore, involved performing a grid indentation of 16 (x-direction) by 25 (y-direction) indents with a spacing of 1.5 μm and targeting a maximum depth of 150 nm.

The tip was calibrated before testing on a standard fused quartz sample, employing a constant strain rate of 0.05.

High-speed mapping using the Express Test available protocol was then performed on a different area of the TBF-1180 steel sample, where EBSD was also conducted. The Express Test allows for rapid and efficient spatial mapping. Each indent typically takes a significantly reduced amount of time (less than five seconds, down to 1 second), encompassing the time for surface approach, surface detection, loading, unloading, and positioning the sample for the subsequent indentation. This mapping utilized an array of 57 ×57 indents in load-control mode, targeting a load of 2.66 mN.

To ensure a high probability of hitting the small available grains, we implemented a sampling criterion that considers, as a first approximation, the diameter (d_p) enveloping the Berkovich-shaped indenter projected geometry (as a function of the depth (h)).

Specifically, we could write that:

$$\frac{h}{r} = \tan(12.95^\circ) \tag{1}$$

$$d_p = 2r = 2\frac{h}{\tan(12.95^\circ)} \tag{2}$$

This study used two-fold reasoning to select the indentation depth from CSM data (selecting the appropriate load in load-controlled mode): (i) avoiding artifacts in indentation data due to tip imperfections, microstructurally induced serrations, and pop-ins at shallow depths, and (ii) sampling following the abovementioned criteria. For the selected 2.66 mN of target load, an average penetration depth of 146.6 nm was achieved, with a spacing of 1.51 μm, in line with the recommendations from Phani et al. on the achievable minimum spacing for nanoindentation [39]. Therefore, a calculated projected probing diameter of 1.3 μm is reported.

The tip area function calibration and load-frame compliance are performed on fused silica samples, similarly to CSM protocols, while employing the dynamical conditions attained by the high-speed protocols, with strain rates approaching orders of 1 1/s. The hardness and elastic modulus for every indent are computed using the standard Oliver & Pharr method.

2.4. Meta-analysis and workflow

The meta-analysis was carried out with R language to perform (i) coordinates matching of the phase maps, (ii) machine learning operations related to image clustering, and (iii) training of supervised prediction models. All computations were performed using 64-bit Windows 11 Home (Intel ® Core™ i5–8250 U CPU @ 1.60 GHz, 1801Mhz 4 Cores, 8 Logical Processors, and 24.00 GB RAM). R Studio is an open-source software and provides a coherent, flexible system for data analysis.

The study delves into the structure-property relationship of the advanced high-strength steel (AHSS) TBF-1180 by juxtaposing the structural phase map obtained from EBSD with the nanomechanical phase maps derived from nanoindentation. Given the complexities of phase analysis in multiphase materials using nanoindentation mapping and clustering, a methodology that employs the conventional statistical approach of probability distribution analysis (PDA/PDF) was adopted. This method assigns properties to phases and accurately fits Gaussian distributions to the maximum depth histogram specific to the nanoindentation grid, as detailed in [21].

Subsequent steps involve, based on structural phases, the refinement of these phase annotations. This is achieved by correlating each nanoindentation point with its corresponding coordinates characterized by EBSD. The primary objective of this methodology is to align two images, each an outcome of distinct characterization techniques. In this context, the images are phase maps, and their correlation is established at approximately 2500 nanoindentation coordinates to derive the material's phase/microstructure (P/M) statistics. Nanoindentation aids in distinguishing between Bainite and Ferrite phases, a distinction that EBSD struggles with due to its inherent limitations. Conversely, EBSD refines the nanoindentation phase mapping by verifying the accuracy of martensite and retained Austenite detection.

Ultimately, the EBSD-validated dataset is employed to train a machine-learning classification model. This model then corrects the values initially misidentified by nanoindentation as either Ferrite or Bainite, ensuring a thorough analysis of the region of interest based on the validated dataset.

Lastly, Inverse Pole Figure (IPF) maps are employed for edge detection. This procedure can be integrated at any workflow stage to segregate the validated dataset from data associated with grain boundaries. A comprehensive overview of this study's workflow is depicted in Fig. 1.

3. Results

3.1. Optical microscopy

Initial insights into the microstructure of the studied TRIP TBF-1180 steel were obtained through the colour tint etching technique [32,33]; in particular, Klemm I etching (which includes the use of saturated sodium thiosulfate and potassium bisulphate) was used—the image of the etched surface and after staining is shown in Fig. 2.

Ferrite, bainite, martensite, and austenite can be observed, as reported in the literature [1]. However, the interpretation highly depends on the metallographer judgment, making bainite and martensite indistinguishable.

3.2. EBSD analysis

The non-etched TBF-1180 sample was used to perform SEM-EBSD analysis. Micro-indentation marks were performed at the Region of Interest (ROI) boundaries to facilitate cross-correlations between the different techniques. In this case, an EBSD area was delimited, as shown in Fig. 3**a**.

EBSD analysis of multiphase steels presents complexities, primarily

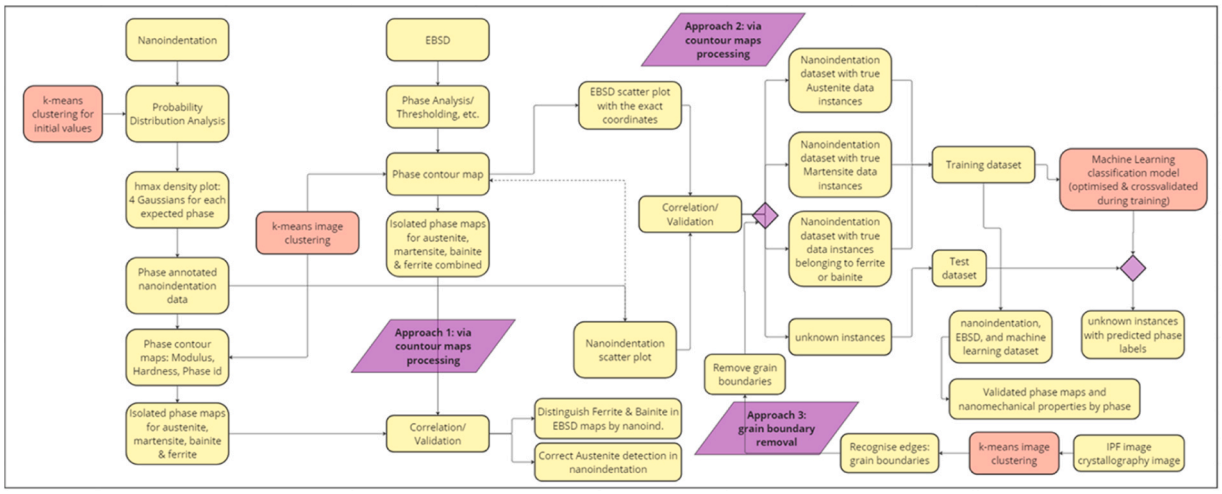

Fig. 1. Mind map of the investigation: the workflow of meta-analysis of ex-situ produced nanoindentation and EBSD data was conducted within the same ROI.

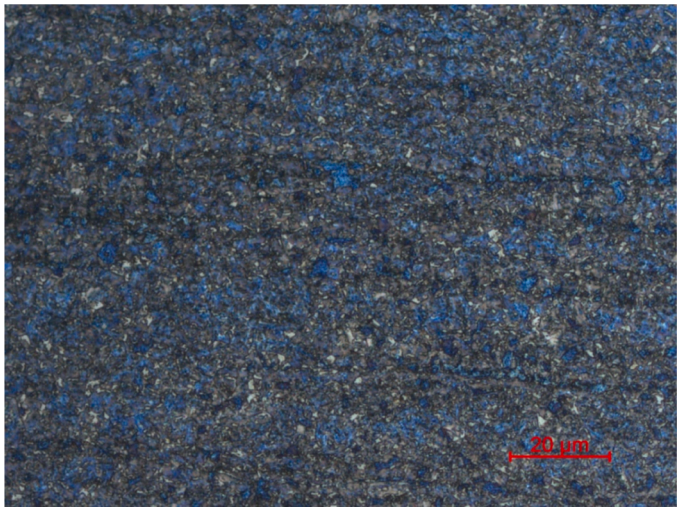

Fig. 2. Microstructure of steel revealed through Klemm I colour tint etching. The ferritic phase was stained with beige, bainite, and martensite, which remained indistinguishable – dark navy blue. The austenite grains and martensite-austenite isles remained white. The average grain size was between 1 and 3 μm.

because many phases/microstructures share similarities. Austenite can be easily distinguished by its FCC lattice. This resemblance between the BCC structure of ferrite, bainite (a micro-constituent from ferrite and cementite, intrinsically sharing characteristics with the ferrite matrix composed by), and martensite (TBC) leads to classification failures. Moreover, there are no means to deconvolute between upper bainite (formed by alternate lamellae of ferrite and cementite) and lower bainite (ferrite matrix with lamellar carbide precipitate).

Nevertheless, their Kikuchi pattern is too similar. Indeed, if the martensite structure is not sufficiently stressed, the Kikuchi pattern will be close to the respective ferrite. A method that can distinguish ferrite and martensite consists of using band contrast, which exploits the different resolutions between the Kikuchi patterns. Kikuchi pattern quality will decrease if the martensite lattice is stressed along a crystallographic direction, while the number of Kikuchi bands typical for ferrite will be lower. The carbide size in the bainite case is minuscule relative to the measurement area. As a result, the final Kikuchi pattern will display bands for both ferrite and cementite [21] [40]. However, the resolution of the ferrite Kikuchi bands will be more pronounced than that of carbides due to their significantly higher quantity, ultimately masking the bainite classification.

In this study, the sample had a fine grain size, and the structures were not easily detectable by the eye. According to the "Re-Classify" ML tool, this hinders phases and microstructure recognition operations. One solution would be to make smaller maps with higher resolution, which may result in electron drift phenomena due to the accumulation of charge on the sample surface from the presence of the carbides.

Nonetheless, considering that martensite possesses low Band Contrast (BC) values, resulting in darker areas on the map, any dark feature with an acicular appearance has been identified as martensite during image analysis. The final phase/microstructure (P/M) image is presented in Fig. 3**b**, where bainite and ferrite remain indistinguishable.

3.3. Nanoindentation analysis and meta-analysis of the ex-situ data outputs obtained in the same ROI

Fig. 4 presents the nanoindentation response from CSM preliminary acquisitions. From the observation of the curves, two main evident phenomena are visible, both being the main reasons for the selection of a target depth for subsequent high-speed mapping of 150 nm: (i) microstructural features being exerted at the very first nanometers of surface, tip apex (20 nm nominal) related artifacts, geometrical errors and serrations, preventing the usage of the region before 80 nm (visible as abrupt changes in the displacement response within the CSM curves) ultimately; (ii) there is no distinction between responses visible from the scatter of the elastic modulus data (as expected being the elastic response affecting the whole material ideally).

Fig. 5 presents the corresponding 2D contour maps for the elastic modulus and hardness. The blue square in the image marks the Region of Interest (ROI) for EBSD and HSNM cross-correlation.

From the observation of Fig. 5, it is noted that a distinguishable similarity pattern can be evidenced between its features and those within the presented EBSD phase map (Fig. 3**b**). This suggests that hardness is a robust descriptor for correlating structure with properties, as detailed in the discussion section, as per the limited extension of the plastic zone (compared to the elastic deformation) promoting a smaller cross-correlation during force transfer to individual microstructures (more negligible substrate/matrix influence) [41]. This is especially true given that steel microstructures typically possess relatively small thicknesses across all three dimensions of the reference volume.

Data analysis employs machine learning algorithms to perform clustering, using the indentation hardness and modulus as descriptors in most cases. Such an approach is not always revealed to be representative of the actual phases/microstructures distribution. As per this study, in which four clusters corresponding to four phases/ microstructures

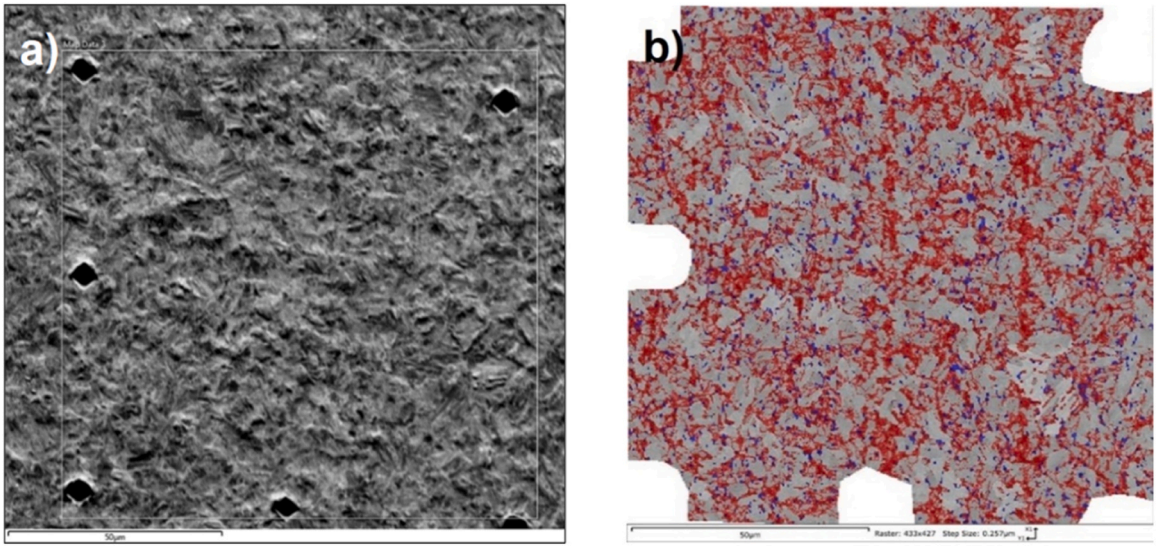

Fig. 3. a) SEM-FSD Image of EBSD analysis area. b) EBSD analysis solved with "Re-classify" tool in AztecCrystal. In this image, different phases and microstructures can be pointed out: austenite (in blue: 4.41%), ferrite (in grey: 61.25%), and martensite (in red:34.34%). The step size is 0.257 μm. The rolling direction is across the vertical axis. White areas are related to the micro indentation marks and are excluded from the analysis.

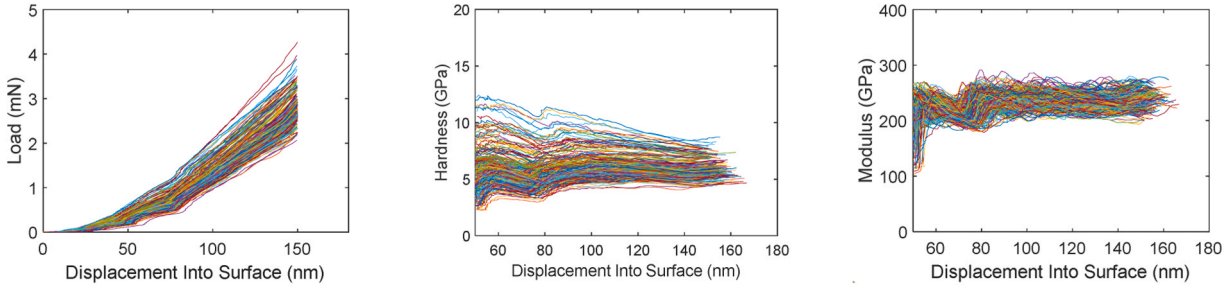

Fig. 4. Load vs. Displacement Into Surface, Hardness vs. Displacement Into Surface, Modulus vs. Displacement Into Surface curves (from left to right) from CSM measurements.

(Ferrite, Bainite, Martensite, and residual Austenite) have been identified, the clustering algorithm doesn't always yield results consistent with theoretical expectations of properties. Indeed, while theoretically, the hardest phase should also have the higher modulus (case of martensite), in a clustering approach, the output might be contradictory considering the dependence and bias due to the high correlation of parameters.

For statistical analysis and cluster allocation, this study focused on the maximum indentation depth, directly corresponding to a nanoindentation raw data (therefore possessing the lowest cross-correlation factor among all the descriptors).

Moreover, each phase has distinct deformation characteristics, allowing for their identification [42–44]. This statistical approach involved fitting four Gaussian curves, each representing a theoretically expected phase in the sample. Data pre-processing involves its translation into a probability distribution (PDA). Initial guessing of mean values and standard deviations was performed using a data-driven approach via k-means clustering. The process is illustrated in the subsequent plot, while the initial values are presented in Table 2.

The probability distribution analysis of the maximum depth histograms, as shown in (Fig. 6), was refined using the expectation maximization optimization algorithm. This step ensures that the analysis avoids suboptimal solutions. Based on this, we identified ratios for each phase, which were then matched and annotated to specific data groups grounded in theoretical knowledge.

Fig. 7 shows density scatter plots within the mechanical property dataspace, showcasing a distinct dense region where the EM-enhanced PDA results are mapped in two dimensions. This dense clustering effectively illustrates the overlap of ferrite and bainite phases, highlighting the challenges in distinguishing them due to their intertwined nature. In addition, the figure contrasts these results with EBSD analysis, which struggles to differentiate between ferrite and bainite in steel. This difficulty arises from their similar body-centered cubic crystal structures and closely related orientation to the parent austenite phase. Both phases appear chemically analogous under EBSD, focusing on crystallography rather than chemical composition, reinforcing the necessity for multiple analytical approaches to study complex steel microstructures. This analysis represents the starting point of the methodology, directly correlating to the lack of distinguishable features visible in Fig. 12c.

Table 3 presents the phase properties based on nanoindentation mapping from the statistical clustering approach with PDA fitting of Gaussian curves and optimized by the EM algorithm.

A contour plot illustrating the mechanical phases was subsequently produced, as seen in Fig. 8. In this plot, each phase is represented by a numerical annotation: 1 for austenite (the softer phase), 2 for ferrite, 3 for bainite, and 4 for martensite (the harder phase).

3.3.1. *Step 1: image correlation*

3.3.1.1. Step 1.1: refinement of phase assumptions. Image correlation is used in the first processing step to obtain a broader overview of surface mapping and use the vast amount of data points provided by the colour maps to refine assumptions about the phase distribution in the sample.

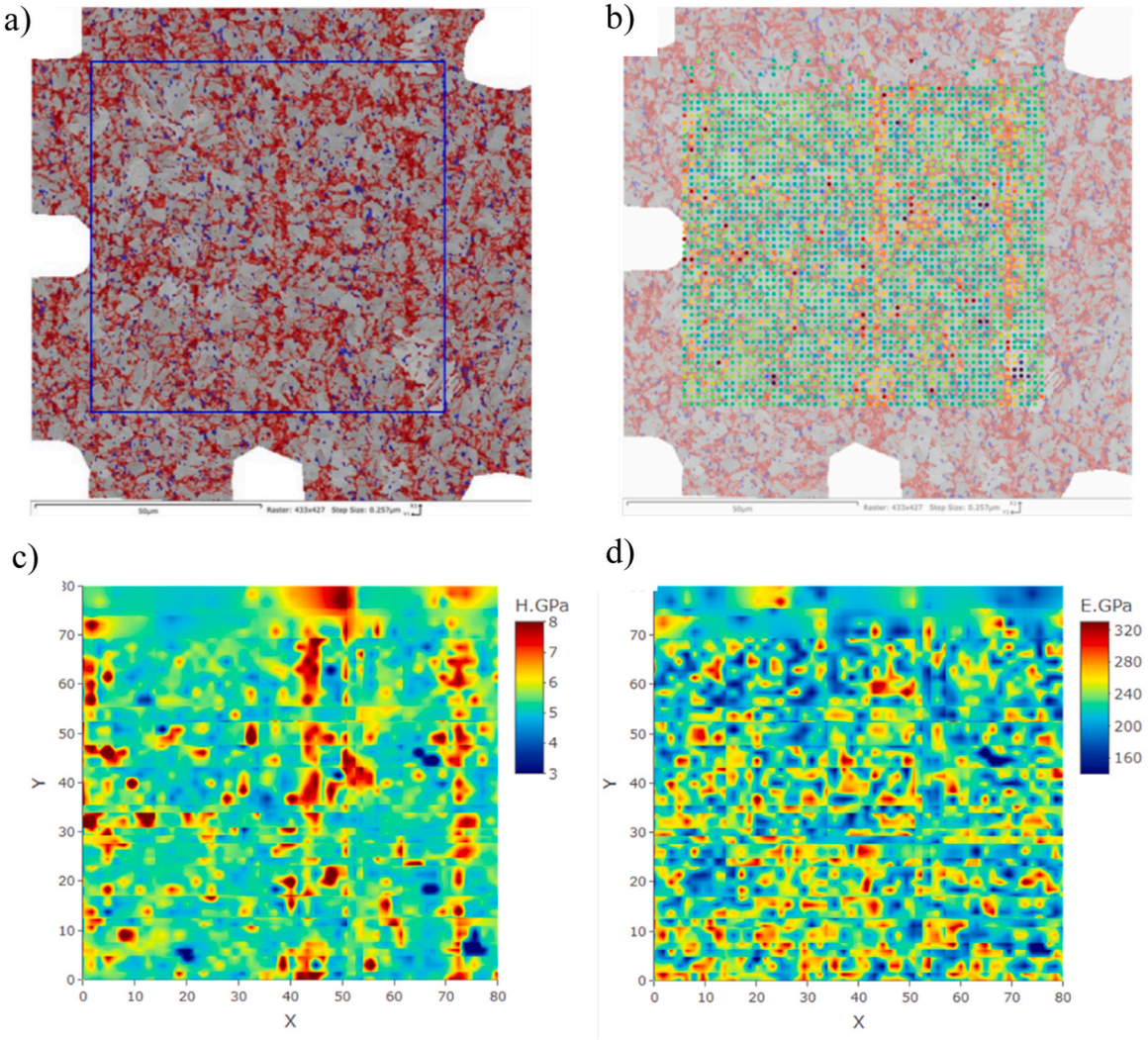

Fig. 5. (a) EBSD map with ROI depicted within the boundaries of the blue square, (b) overlap of the nanoindentation hardness 2D scatter plot and EBSD map in the same ROI, (c) indentation hardness map, (d) indentation modulus map. X and Y coordinates are presented in μm.

Table 2
Initial parameters of mean value (mu) and standard deviation (sd) for maximum depth parameter were calculated by single parameter k-means clustering. In contrast, the final parameters were derived after fitting the Gaussian PDA after the EM step.

Cluster	Depth mu (nm)	Depth sd (nm)	Depth mu (nm) [after EM step]	Depth sd (nm) [after EM step]	Phase annotation	Phase ratio (%)
1	154.4	5.7	151.2	4.9	Ferrite	38.7
2	145.1	3.4	147.4	4.8	Bainite	39.5
3	127.2	6.3	130.9	8.6	Martensite	19.9
4	275.8	60.6	204.6	63.3	Austenite	1.9

By exploiting nanoindentation maps and EBSD maps, the following combined maps (Fig. 9) were created from the overlap of those figures, averaging the RGB values for each matching coordinate.

The corresponding images were processed using the R programming language to integrate the findings from both characterization techniques. Given the vast array of color shades in the original images (amounting to tens of thousands), a direct analysis was daunting. The k-means clustering method is employed, allowing the categorization of the color shades into three principal clusters, each representing an AHSS TRIP phase.

The rationale behind employing k-means clustering was to streamline the color spectrum. By doing so, the numerous shades in the EBSD phase/microstructure (P/M) maps were condensed down to just ten. Despite this simplification, these shades retained the image's inherent detail. These latter were then grouped into three primary colors: red, blue, and grey, each denoting a distinct phase (Fig. 10). These refined, color-coded maps were then used in subsequent stages to align them with the nanoindentation phase map.

3.3.1.2. Step 1.2: alignment of nanoindentation and EBSD maps. Aligning the results from both characterization techniques requires multiple steps centered around comparing phases via their coordinates:

1. Begin with the image obtained from nanoindentation.
2. Refine this image to distinguish individual data points, which facilitates the extraction of phase statistics.

For the nanoindentation phase map, clustering distinguishes the colors indicative of each phase, leading to clear mechanical phase maps. The processing method for the nanoindentation phase map parallels that of the EBSD image. The k-means clustering technique segregates the image into 18 unique colors, retaining the original image's intricacy.

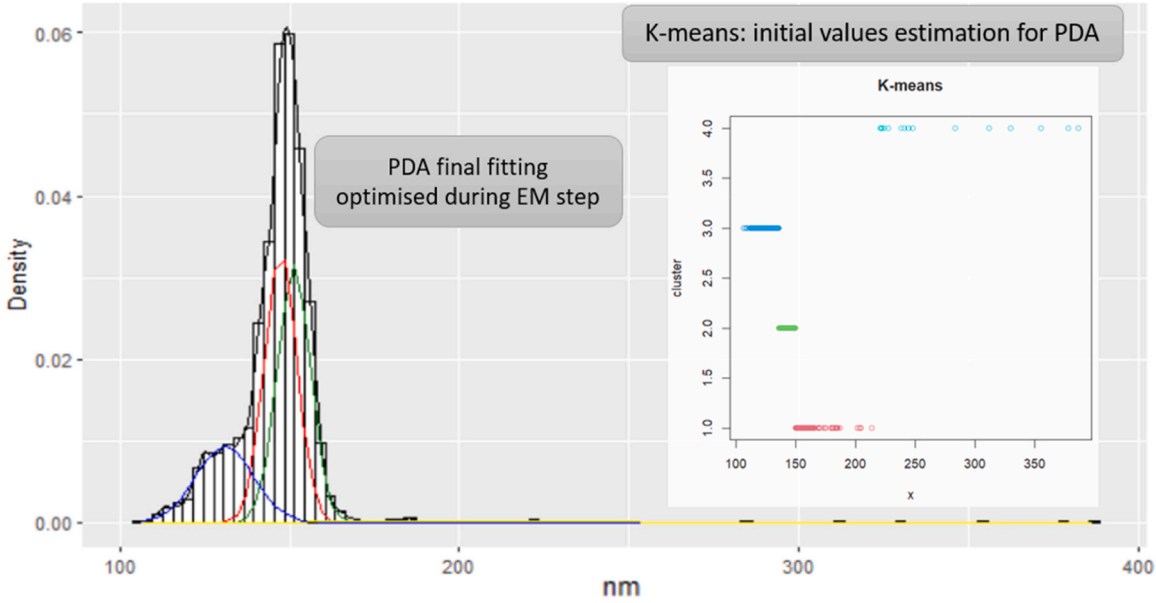

Fig. 6. PDA analysis and fitting of histogram plot of the maximum indentation depth after the EM step; initial values for the EM step were provided via k-means clustering.

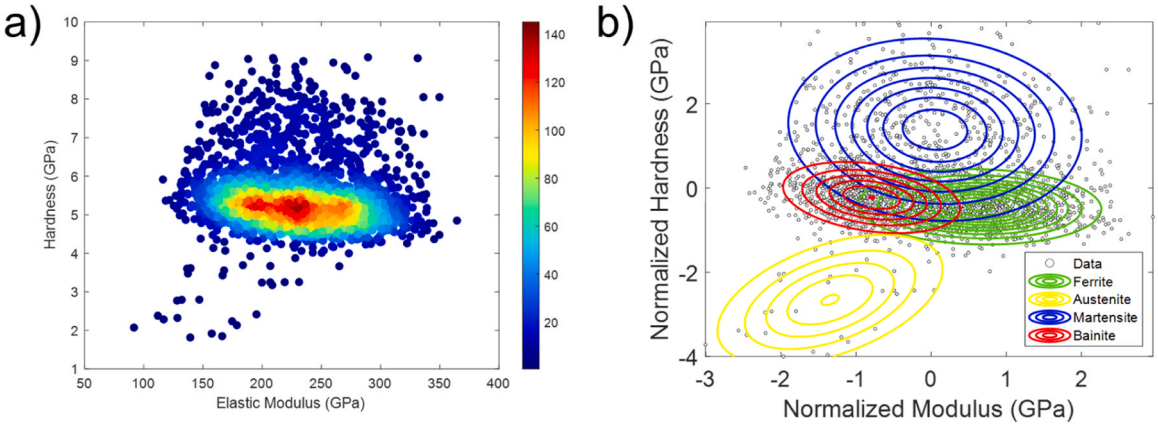

Fig. 7. a) Modulus vs. Hardness plots elucidating the relationship between probed values in the mechanical properties space. b) 2D Gaussian representation of the PDA EM-optimized data fitting within the Hardness vs. Elastic Modulus (normalized values) space: the phase statistics are highlighted following Fig. 6 color coding.

Table 3
Phase statistics generated from nanoindentation mapping and PDA optimized by EM step.

	Martensite	Bainite	Ferrite	Austenite
E **(GPa)**	236.1 ± 44.1	230.6 ± 44.8	226.3 ± 46.1	172.2 ± 52.6
H **(GPa)**	7.1 ± 1.0	5.5 ± 0.3	4.9 ± 0.3	3.1 ± 1.1

These 18 colors are then grouped into four primary shades, each representing a phase: martensite, austenite, bainite, or ferrite.

Subsequently, images for each of these phases were isolated. These isolated images were then superimposed onto the structural phase map from EBSD. Only data points with identical coordinates in both maps were retained in the final images, as shown in Fig. 11. Precisely, 21.12% of the data points matched martensite, 1.12% for austenite, and 56.16% for a combination of ferrite and bainite. Any unmatched data points were excluded from the final representation.

3.3.2. Step 2: Data correlation with nanomechanical properties for each nanoindentation coordinate

Refining the observations to match the coordinates of the actual nanoindentation events is essential to improve the accuracy of the P/M correlation approach. Contour maps may contain intermediate data representing the mean value between two color shades. This can fill in missing data but also introduces potential bias in phase correlations. This bias arises from the inclusion of synthetic data during contour plot creation. Leveraging the actual data from nanoindentation mapping (2519 points) and the exact correspondence of the coordinates in the EBSD map, it is possible to increase confidence in correlating the two maps. This step also facilitates validating the phase ratio and distribution in the specified ROI. Furthermore, it allows the extraction of the P/M statistics related to the nanomechanical properties. Fig. 12 shows the scattered maps obtained through nanoindentation and the combined map produced by correlating it with the EBSD map.

EBSD correlation was used to refine the nanoindentation phase statistics and curate the data based on the actual structural phase detected by diffraction. The corresponding statistics for the phases identified by EBSD are presented below (Table 4), first using the original EBSD labels and then using nanoindentation feedback to separate Bainite from

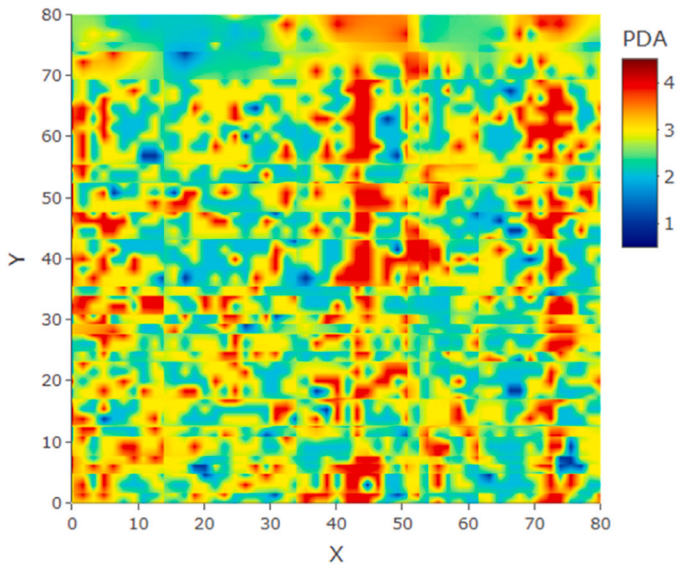

Fig. 8. Mechanical phase map produced by PDA analysis for the preliminary annotation of nanoindentation data. X and Y coordinates are presented in μm.

Ferrite.

The procedure to deconvolute the two latter phases based on the mechanical response is illustrated below. Thus, the validation process includes using nanoindentation feedback on EBSD phase annotation to distinguish ferrite (softer) from bainite (harder), as shown in Fig. 13 and Table 5. At the same time, EBSD provides accurate validation of which mechanical phases agree with the structural phase distribution and enables the calculation of the mean values of their nanomechanical properties).

3.3.3. *Step 3: train a supervised machine learning model using the validated and curated combined nanoindentation-EBSD dataset to classify the unknown instances of nanoindentation*

Discrepancies were noticed when comparing the EBSD and nanoindentation data for the bainite and ferrite phases. Some nanoindentation results expected to identify as Bainite or Ferrite were mapped as martensite or austenite by the EBSD structural map.

Leveraging the insights from the validated dataset, a supervised classification model was implemented to classify the data that did not align between the two characterization methods. We trained a Random Forest Machine Learning model, setting the entry parameter to 6. This setting yielded the highest training accuracy of 61.5%. The model's training and prediction processes relied on parameters like maximum depth, Elastic modulus, hardness, and an assigned label (validated by EBSD). One advantage of the Random Forest algorithm is that it doesn't require data pre-processing or scaling since it's not distance-based. During the model's training phase, we introduced resampling and applied 20-fold cross-validation, repeated ten times, to enhance prediction accuracy.

The model's predictions for the test (unvalidated) dataset showed that 86.7% was martensite. In contrast, 0.9% was incorrectly identified as bainite, another 0.9% as ferrite, and 11.5% was identified as austenite. These results align with our expectations given the nature of the classification problem: the dataset with unidentified instances primarily came from bainite and ferrite misclassifications via nanoindentation. As such, we anticipated most observations to be martensite or austenite—austenite is expected to be a minor portion based on a 1:9 ratio compared to martensite in the EBSD phase distribution. This prediction distribution strengthens our confidence in the model's accuracy.

In a further test on the uncorrelated data, consisting of 111 observations, the model successfully categorized the majority into Martensite and Austenite. Only two instances were misclassified as Bainite and Ferrite. Fig. 14 illustrates the nanoindentation phase scatter map, depicting its evolution from initial PDA clustering to its alignment with the structural phase map (post-validation) and the application of the classification model. Meanwhile, Table 6 documents the resultant properties by phase. It's worth noting that this trained model can be repurposed, eliminating the need to reconstruct a machine-learning model from scratch. It offers a valuable tool for analyzing nanomechanical data and conducting phase identification based on a knowledge base correlating structural and mechanical data. The consistent accuracy of the model suggests no overfitting, further reinforcing its potential to predict unverified P/M instances accurately.

3.3.4. *Step 4: identification of the contribution of grain boundaries to the nanomechanical properties*

The final step of the proposed methodology was to take advantage of the rest of the EBSD data that could be used to extract more information on the phase correlation with the nanomechanical properties, for example, using the IPF map, which depicts the grain orientation in the ROI. The image was read as a dataset to perform edge detection and extract the grain boundary coordinates using the IPF image. The IPFX map image was converted to grayscale to conduct edge detection as a preparation step. The edge detection confirmed the grain size population provisionally evaluated for the selected indentation depth validation. Indeed, two classes of grain sizes are present in this type of steel for bainite and austenite, varying between 1 and 3 μm, while that of the ferritic grains varies between 5 and 10 μm. For the same material (same processing parameters and same constitutive phases), the values are also backupped by Furnémont et al. [45]. Then, the subsequent grayscale image was clustered in 12 colors, from which the shades were allocated to grain boundaries and matrix. After refining the data based on the coordinates of the grain boundaries (Fig. 15), the nanoindentation data corresponding to the nanoindentation of a pure microstructure were

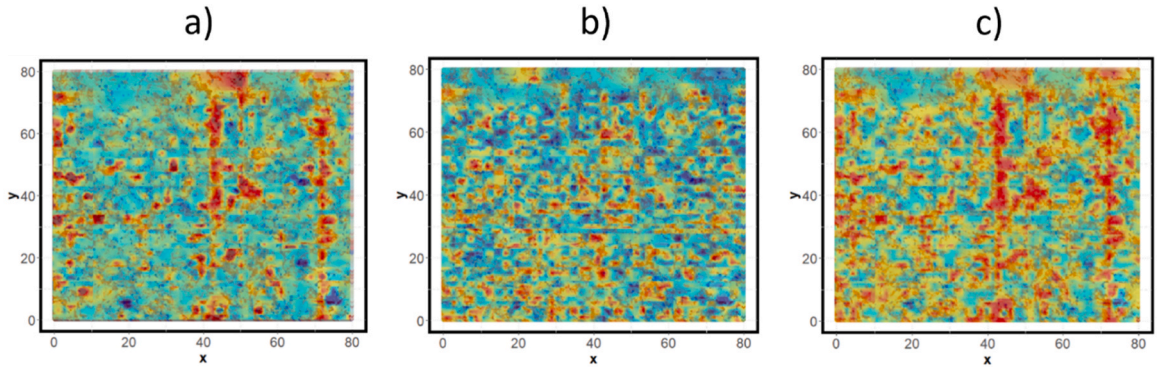

Fig. 9. Combined EBSD and nanoindentation phase maps; a) Hardness over EBSD, b) Modulus over EBSD, c) Phase over EBSD. X and Y coordinates are presented in μm.

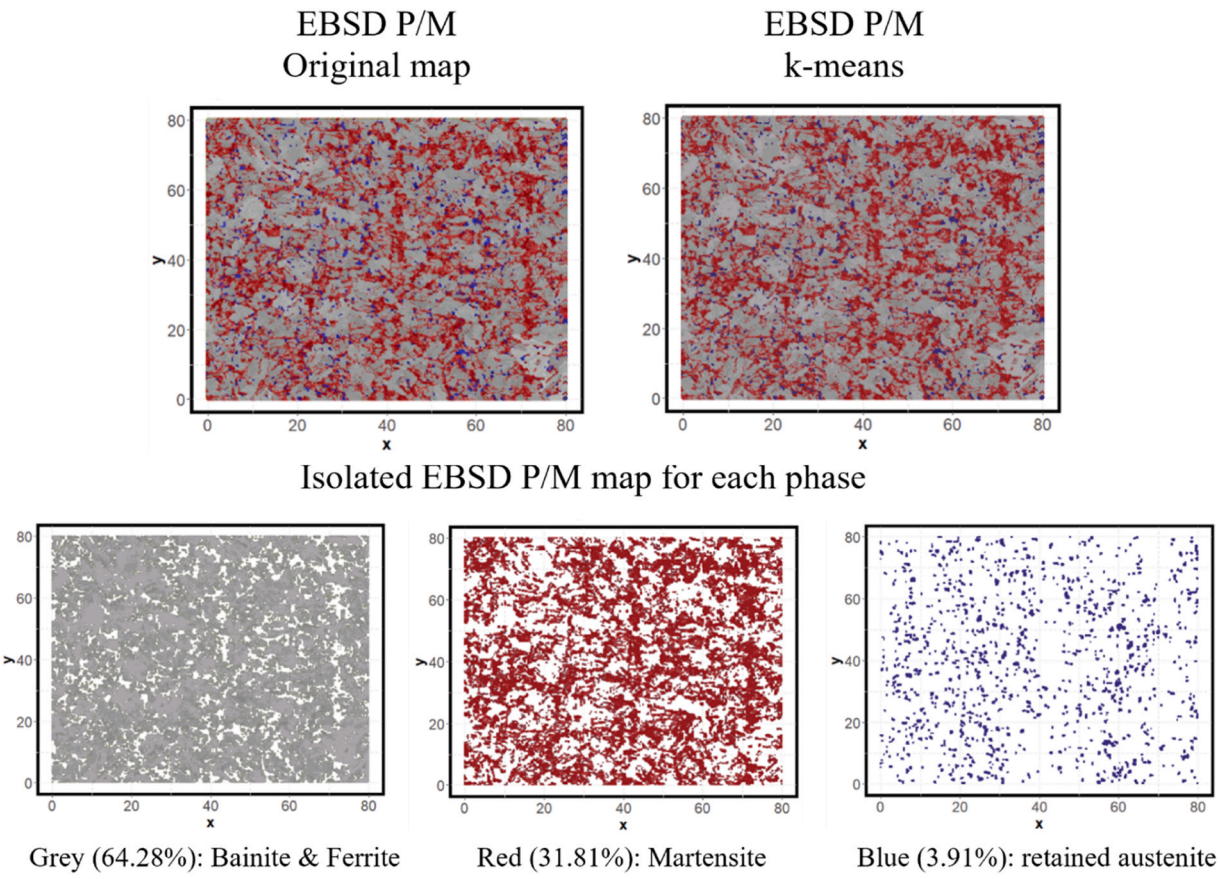

Fig. 10. EBSD P/M original vs clustered map and individual P/M maps for each structural phase. X and Y coordinates are presented in μm.

reduced to 36.1% of the size of the initial nanoindentation dataset.

The nanomechanical properties, categorized by each phase, are detailed below (Table 7). These properties were derived after correlating them with EBSD data, removing grain boundaries, and deconvoluting Ferrite and Bainite using nanoindentation. The grain boundary removal process significantly reduced the dataset from the original 2519 nanoindentation data points to 907.

Table 8 summarises the phase properties after all validation steps (nanoindentation, EBSD, machine learning supervision, removal of grain boundaries). Classification of the false data classified as Bainite or Ferrite by PDA analysis of nanoindentation data were predicted by training and using a random forest model, as described in step 3 in Section 3.3.3.

4. Discussion

4.1. Limitations and sources of bias for ex-situ correlation of characterization phase map outputs corresponding to the same ROI

The proposed methodology presents a stepwise approach, combining the knowledge obtained for the same ROI by two characterization techniques, utilizing one structural characterization to validate the outputs of a mechanical characterization in phase mapping. The modular approach can be applied on demand to treat similar mapping outputs amongst other characterization methods or to combine more than two outputs generated in the same ROI. However, some sources or factors that can introduce bias in image correlation should be discussed.

When a user is conducting a pixel-wise image comparison, if the user does not pick precisely the same (x, y) coordinates to compare the two image mapping outputs or introduces artificial (x, y) coordinate shift after cropping the two images of the mechanical characterization and the diffraction map. This can have an impact by introducing a drift associated with the image preparation for performing the subsequent one-by-one correlation in a pixel-wise comparison, thus affecting the correlation accuracy.

Another limitation is the image quality used for the subsequent analysis. If the quality is poor, then the image dataset will consist of fewer data points by each, i.e., pixels per micrometer distance of (x, y), which results in fewer chances for the two different image datasets of the phase maps to match the exact pairs of (x, y) coordinates and to produce a more precise image correlation. Also, when correlating coordinates using a coding environment, to match the coordinates, a rounding process to a specific decimal number can be applied to simplify the correlation process. This inconsistency can be considered if precision issues arise, and more advanced analysis should be accounted for to overcome such bottlenecks. Moreover, when contour plots are compared, the synthetic values used to formulate the contour plot between subsequent locations typically use an average value that might not represent the actual materials' properties due to the actual size variation of individual P/M, thus increasing the uncertainty of the correlation.

The size of the dataset and the presence of grain boundaries could be another source of potential bias, specifically when the size of the dataset is relatively small, which cannot only affect the validation outcomes but also reduce the statistically representative character of the phase ratio quantification in the investigated ROI. In the present study, using about 2500 data points from nanoindentation mapping could be considered a sufficient statistical sample. However, proportionally larger datasets can increase confidence in the phase mapping statistics.

Recently, the challenge of filtering data corresponding to grain boundaries is a central aspect of this research. Our developed procedure addresses this challenge by considering the effects of removing

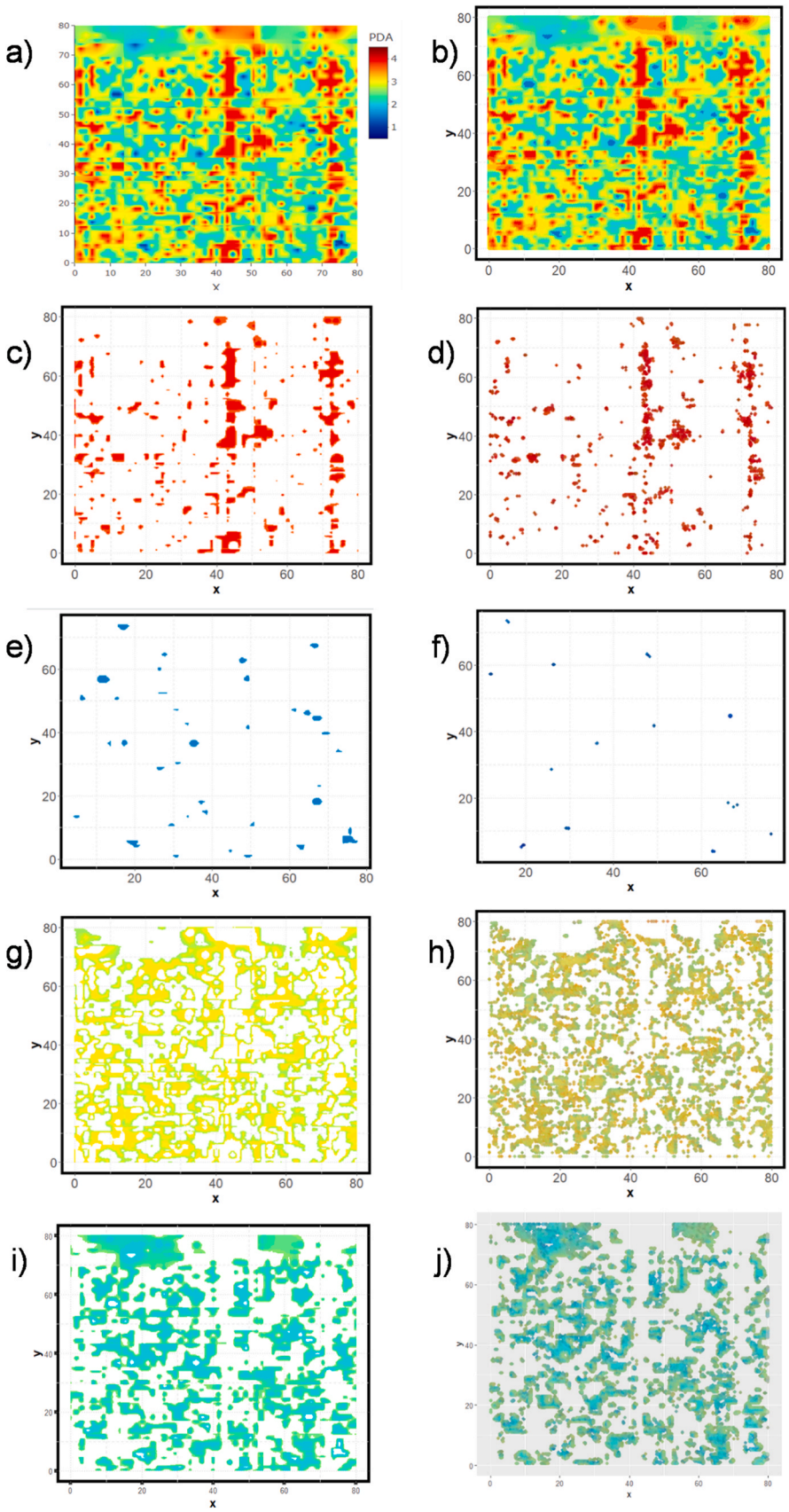

Fig. 11. (a) original nanoindentation phase map image, (b) clustered image, (c) nanoindentation martensite map, (d) combined nanoindentation-EBSD martensite map, (e) nanoindentation austenite map, (f) combined nanoindentation-EBSD austenite map, (g) nanoindentation bainite map, (h) combined nanoindentation-EBSD bainite map, (i) nanoindentation ferrite map, (j) combined nanoindentation-EBSD ferrite map. X and Y coordinates are presented in μm.

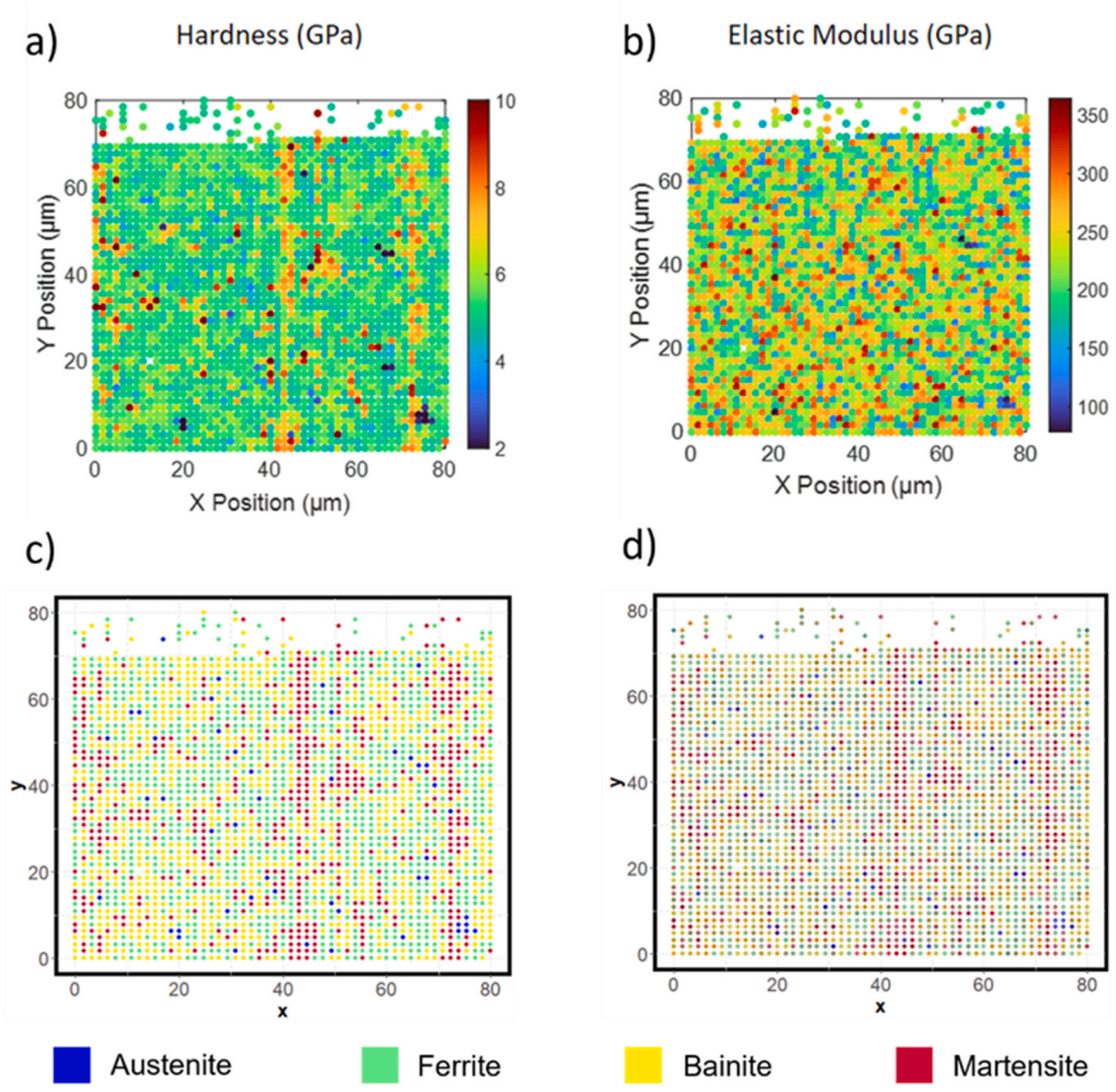

Fig. 12. Nanoindentation scatter plots: (a) hardness map, (b) indentation modulus map, (c) phase map, (d) overlayed nanoindentation phase scatter map with EBSD (2519 data points in total). X and Y coordinates are presented in μm.

Table 4
Phase statistics derived from coordinate (x,y) annotation by EBSD. *Phase ratio here refers to the amount of data from nanoindentation observations labeled as specific phases and differs from EBSD phase ratio quantification.

EBSD	Martensite	Batinite & ferrite combined	Austenite
E (GPa)	227.9 ± 46.2	230.0 ± 45.9	221.4 ± 47.5
H (GPa)	5.6 ± 1.1	5.5 ± 1.0	5.3 ± 0.8
Phase ratio (%)*	23.1	79.4	3.5

* Phase ratio here refers to the amount of data from nanoindentation observations labeled as specific phases and differs from EBSD phase ratio quantification.

substantial areas where boundaries could influence the indentation response, as depicted in Fig. 15. Moreover, the influence of the surrounding microstructural context on the sole nanoindentation data is undeniable. These effects significantly impact the correlation with electron backscatter diffraction (EBSD) data, necessitating extensive filtering of regions surrounding grain boundaries.

Despite meticulous efforts, the intrinsic properties of the probed volume and existing material defects remain unavoidable factors influencing the results. However, strategies discussed in the paper aim to mitigate these effects by carefully correlating the data. Specifically, correlations are primarily based on contact depth, which directly relates to the hardness response of the material. This parameter offers a relatively confined influence within the material compared to other nanoindentation measurements.

4.2. Technological impact of the phase quantification and scientific soundness of the approach

A complete identification and quantification of different phases for AHSS is a mandatory step to advance the AHSS technology. Still, the lack of inclusive characterization techniques is becoming evident while the market moves to 3rd Generation AHSS. In addition, such methodologies are required in another application, specifically in detecting Unreacted Retained Austenite (URA) in ADI (Austempered Ductile Iron) cast iron. URA is detrimental to the material's mechanical properties because it is a metastable phase that can transform in martensite and lead to cracks and failure of the component. Otherwise, detecting and quantifying URA by separating it by retained high-carbon stable austenite is almost

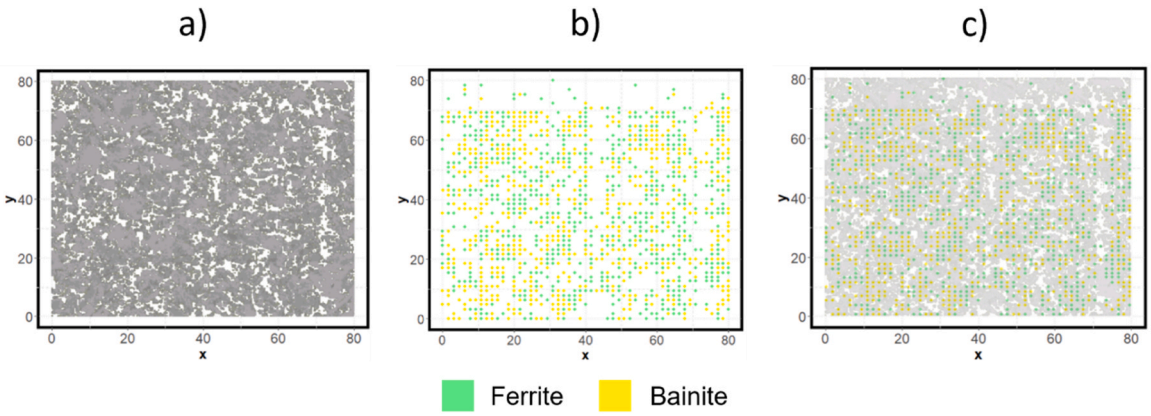

Fig. 13. (a) Isolated EBSD map of the bainite and ferrite region, (b) scatter map of the nanoindentation Bainite and Ferrite region, and (c) combined nanoindentation and EBSD map of Bainite and Ferrite region.

Table 5
Phase statistics derived from coordinate (x, y) annotation by combined phase analysis data from nanoindentation and EBSD.

Validation of EBSD grey ROI by nanoindentation	Martensite	Bainite	Ferrite	Austenite
E **(GPa)**	227.9 ± 46.2	232.1 ± 44.1	226.7 ± 46.4	221.4 ± 47.5
H **(GPa)**	5.6 ± 1.1	5.4 ± 0.3	4.9 ± 0.3	5.3 ± 0.8
Phase ratio (%)	23.1	39.3	40.1	3.5

impossible, which is a desired phase. In this study, the correlation of a mechanical and diffraction characterization method to assess the exact ROI and leveraging the computational intelligence enabled us to reach a validated dataset and a model that can efficiently support the classification of grain boundaries, martensite, and austenite. At the same time, it is possible to distinguish ferrite and bainite based on the established structure-property relationships in the machine learning model.

Moreover, considering that the phase ratio of individual microstructures in steels is not readily available from steelmakers, the precise examination of the phase ratio with the proposed methodology can help overcome this limitation and knowledge gap. It should be noted that the phase ratios quantification compared to other TRIP steels studied in literature might disagree with this study; for example, the TRIP steels in the study of Jacques et al. do not contain any fraction of martensite, which is something connected to the chemistry and the thermal history [46] or use SEM assisted quantification, which can be limited under the imaging conditions adopted [47] where for example a higher phase ratio of austenite over martensite was detected. However, the precision of the detection, according to the present study, utilizes more data than occasionally used in literature and presents a data-informed approach utilizing the outputs of two techniques to assess the structure and properties of these steels in a more objective outcome. Often, when EBSD and nanoindentation outputs are combined, there is not considered precisely what the grain boundary contribution to individual P/M nanomechanical properties would be [48], where it is estimated that the austenite properties are higher than ferrite properties in the studied

Table 6
Nanomechanical properties after the phase annotation results are revised based on EBSD and Machine Learning.

	Martensite	Bainite	Ferrite	Austenite
E **(GPa)**	229.1 ± 46.7	232.0 ± 44.2	226.7 ± 46.4	222.3 ± 48.4
H **(GPa)**	6.0 ± 1.4	5.4 ± 0.3	4.9 ± 0.3	5.3 ± 0.8
Phase ratio (%)	44.5%	25.6%	25.3%	4.6%

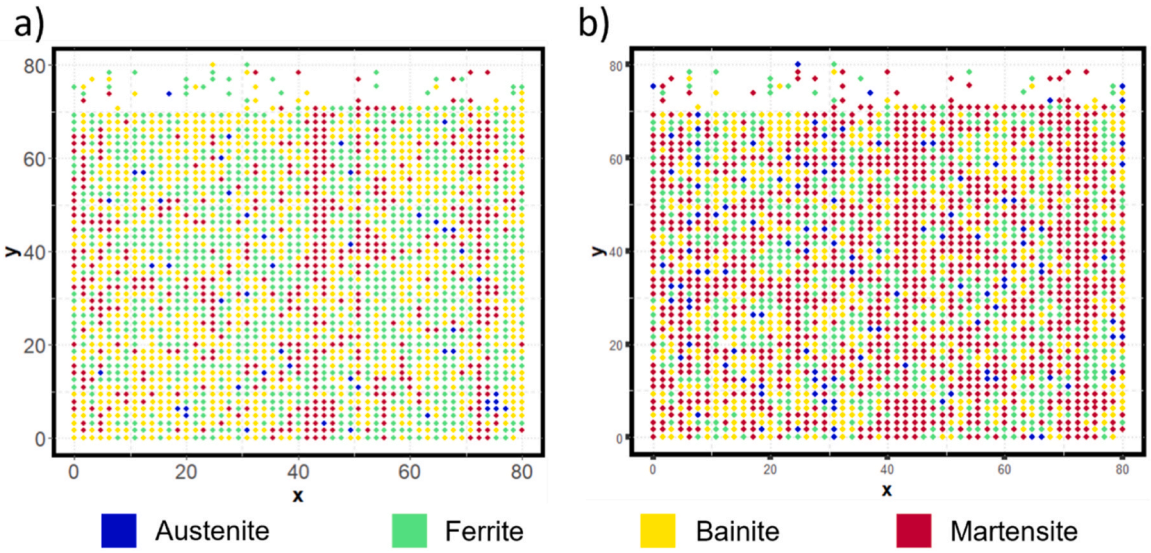

Fig. 14. (a) Initial nanoindentation scatter plot, (b) revised nanoindentation scatter plot, validated by EBSD and supervised by the RF machine learning model. X and Y coordinates are presented in μm.

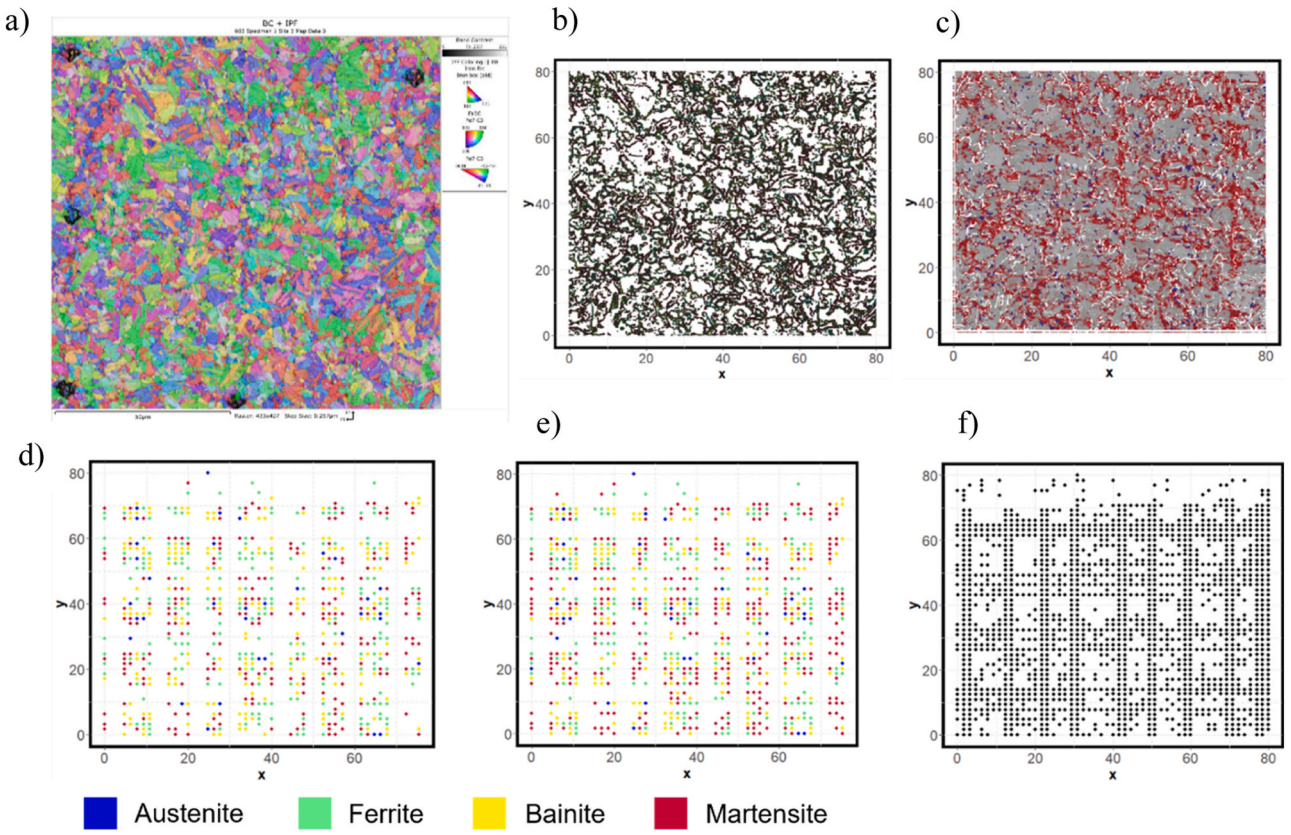

Fig. 15. (a) IPF map from EBSD, (b) edge detection of the grain boundaries in IPF image within ROI, (c) clean EBSD phase map from grain boundaries, (d) initial nanoindentation scatter pattern with grain boundaries removed, (e) nanoindentation scatter pattern overlaid by EBSD and with grain boundaries removed and prediction of unvalidated values with machine learning (36.1% of initial raw data), (f) nanoindentation scatter corresponding to grain boundary location of indents. X and Y coordinates are presented in μm.

Table 7
Phase statistics following the validation of nanoindentation by EBSD and after the removal of grain boundaries (used as training dataset).

Phase	Martensite	Bainite	Ferrite	Austenite	Grain Boundaries
E **(GPa)**	236.5 ± 42.6	228.9 ± 45.7	225.4 ± 45.2	163.3 ± 52.8	229.5 ± 46.5
H **(GPa)**	7.1 ± 1.0	5.4 ± 0.3	4.9 ± 0.3	2.8 ± 1.1	5.5 ± 1.1

Table 8
Phase statistics following the validation of nanoindentation by EBSD and after removing grain boundaries after supervised learning of unclassified instances.

Phase	Martensite	Bainite	Ferrite	Austenite	Grain Boundaries
E **(GPa)**	231.8 ± 43.8	229.2 ± 45.8	225.2 ± 45.3	210.4 ± 51.7	229.5 ± 46.5
H **(GPa)**	5.9 ± 1.3	5.4 ± 0.3	4.9 ± 0.3	5.7 ± 1.2	5.5 ± 1.1
Phase ratio (%)	41.7%	25.2%	26.7%	6.4%	—

dual-phase steel, without any attribution of the nanomechanical properties measured to the grain boundaries. However, in the latter study [47], where the grains' existence has been taken into consideration, the hardness ranking of the P/M is quite similar to these study outcomes at the final stage of the proposed methodology (Table 8), where the ferrite presented the lower hardness, and martensite the higher. In contrast, Bainite and Retained Austenite have similar hardness, varying within the standard deviation.

In addition, it is essential to note that in most cases, the measurements of the nanomechanical properties are affected by considerable variation of the reported literature values due to the effects of anisotropy [14,49–51], roughness, grain boundaries [52], sample preparation [53], neighboring constituents, residual stress [54], pile-up, time-dependent deformation, orientation, crystal plasticity, and hydrostatic stress [55]. This study has tackled several aspects; the innovative high-speed nanoindentation protocol, characterized by up to one indent per second, minimizes and even nullifies time-dependent effects on the measurement, such as thermal drift, creep or other time-dependent deformation phenomena that occur during loading. In contrast, using EBSD provided information about orientation, anisotropy, grain boundaries, and neighboring constituents, which have increased the credibility of the advanced high-strength TRIP steel evaluation.

Finally, since in nanoindentation, the contact area is lower than the average grain size, from an industrial scale-up perspective, these outcomes can help metallurgists understand both micro- and macro-mechanical properties, wherein indents have more significant contact areas and two or more grains can be intercepted in a single load.

5. Conclusions

This study successfully demonstrated the efficacy of integrating nanoindentation and EBSD for enhanced phase mapping, addressing

nanoindentation's challenge in retained austenite detection. At the same time, nanoindentation enabled the differentiation between Bainite and Ferrite, which was traditionally a limitation due to their similar BCC structures in EBSD. EBSD analysis enhanced the overall accuracy by validating martensite and retained Austenite predictions. Our approach introduced a statistical analysis for accurate phase mapping. It leveraged a validated dataset to train a machine-learning model for more precise classifications when there is uncertainty during phase segmentation. This combination optimized the region of interest analysis. It established a reusable dataset and machine-learning model for similar steel grades, presenting a promising framework for steel nanoscale design and pattern analysis of processing footprint.

Anyway, further improvements are needed to reduce the standard deviation of values. Defects, voids, residual stress, and surrounding phases/microstructures negatively affect measurements' accuracy. It is arduous to manage these phenomena from both experimental and statistical points of view.

CRediT authorship contribution statement

Georgios Konstantoupoulos: Writing – original draft, Visualization, Software, Methodology, Investigation, Formal analysis, Conceptualization. **Edoardo Rossi:** Writing – review & editing, Visualization, Supervision, Investigation, Formal analysis. **Federico Bruno:** Writing – original draft, Visualization, Methodology, Investigation, Formal analysis. **Mauro Palumbo:** Writing – review & editing, Supervision, Resources, Formal analysis. **Marco Sebastiani:** Writing – review & editing, Supervision, Resources, Funding acquisition, Formal analysis. **Luca Belforte:** Writing – review & editing, Supervision, Resources, Funding acquisition, Formal analysis. **Gianluca Fiore:** Visualization, Methodology, Investigation. **Costas Charitidis:** Writing – review & editing, Supervision, Resources, Funding acquisition, Formal analysis, Conceptualization.

Declaration of Competing Interest

The authors declare that they have no known competing financial interests or personal relationships that could have appeared to influence the work reported in this paper.

Data Availability

Data will be made available on request.

Acknowledgments

This research was funded by the EU H2020 Project "Harmonisation of EU-wide nanomechanics protocols and relevant data exchange procedures, across representative cases; standardization, interoperability, data workflow" (NanoMECommons) under Grant Agreement No. 952869. Support from the Project CH4.0 under the MUR program "Dipartimenti di Eccellenza 2023–2027" (CUP: D13C22003520001) is acknowledged.

References

[1] AHSS Application Guidelines - WorldAutoSteel, ⟨https://ahssinsights.org/metallurgy/steel-grades/3rdgen-ahss/transformation-induced-plasticity-trip/⟩), (2023).
[2] A. Dimatteo, G. Lovicu, M. Desanctis, R. Valentini, A. Solina, Microstructures and properties of TRansformation Induced Plasticity steels, La Metallurgia Italiana, 2006.
[3] M.I. Latypov, S. Shin, B.C. De Cooman, H.S. Kim, Micromechanical finite element analysis of strain partitioning in multiphase medium manganese TWIP+TRIP steel, Acta Mater. 108 (2016) 219–228, https://doi.org/10.1016/j.actamat.2016.02.001.
[4] C. Charitidis, M. Sebastiani, G. Goldbeck, Fostering research and innovation in materials manufacturing for Industry 5.0: The key role of domain intertwining between materials characterization, modelling and data science, Mater. Des. 223 (2022) 111229, https://doi.org/10.1016/j.matdes.2022.111229.
[5] W.C. Oliver, G.M. Pharr, An improved technique for determining hardness and elastic modulus using load and displacement sensing indentation experiments, J. Mater. Res 7 (1992) 1564–1583, https://doi.org/10.1557/jmr.1992.1564.
[6] E. Enríquez, A. del Campo, J.J. Reinosa, G. Konstantopoulos, C. Charitidis, J. F. Fernández, Correlation between structure and mechanical properties in α-quartz single crystal by nanoindentation, AFM and confocal Raman microscopy, J. Mater. Res. Technol. 26 (2023) 2655–2666, https://doi.org/10.1016/j.jmrt.2023.08.041.
[7] Z. Zhang, D. Bellisario, F. Quadrini, S. Jestin, F. Ravanelli, M. Castello, X. Li, H. Dong, Nanoindentation of Multifunctional Smart Composites, Polym. (Basel) 14 (2022), https://doi.org/10.3390/polym14142945.
[8] E. Bassini, G. Marchese, A. Sivo, P.A. Martelli, A. Gullino, D. Ugues, Effect of Cold Rolling on Microstructural and Mechanical Properties of a Dual-Phase Steel for Automotive Field, Materials 15 (2022), https://doi.org/10.3390/ma15217482.
[9] J.C. Capricho, K. Prasad, N. Hameed, M. Nikzad, N. Salim, Upcycling Polystyrene, Polymers 14 (2022), https://doi.org/10.3390/polym14225010.
[10] R. Wagner, R. Lehnert, E. Storti, L. Ditscherlein, C. Schröder, S. Dudczig, U. A. Peuker, O. Volkova, C.G. Aneziris, H. Biermann, A. Weidner, Nanoindentation of alumina and multiphase inclusions in 42CrMo4 steel, Mater. Charact. 193 (2022), https://doi.org/10.1016/j.matchar.2022.112257.
[11] E. Borisenko, D. Borisenko, I. Bdikin, A. Timonina, B. Singh, N. Kolesnikov, Mechanical characteristics of gallium sulfide crystals measured using micro- and nanoindentation, Mater. Sci. Eng.: A 757 (2019) 101–106, https://doi.org/10.1016/j.msea.2019.04.095.
[12] H.J. Qi, K.B.K. Teo, K.K.S. Lau, M.C. Boyce, W.I. Milne, J. Robertson, K.K. Gleason, Determination of mechanical properties of carbon nanotubes and vertically aligned carbon nanotube forests using nanoindentation, : J. Mech. Phys. Solids (2003) 2213–2237, https://doi.org/10.1016/j.jmps.2003.09.015.
[13] M.C. Taboada, M.R. Elizalde, D. Jorge-Badiola, Austempering in low-C steels: microstructure development and nanohardness characterization, J. Mater. Sci. 54 (2019) 5044–5060, https://doi.org/10.1007/s10853-018-3159-6.
[14] P. Burik, L. Pesek, P. Kejzlar, Z. Andrsova, P. Zubko, Effect of crystallographic orientations of grains on the global mechanical properties of steel sheets by depth sensing indentation, in: J Phys Conf Ser, Institute of Physics Publishing, 2017, https://doi.org/10.1088/1742-6596/790/1/012003.
[15] M.A. Valdes-Tabernero, R.H. Petrov, M.A. Monclus, J.M. Molina-Aldareguia, I. Sabirov, The effect of soaking time after ultrafast heating on the microstructure and mechanical behavior of a low carbon steel, Mater. Sci. Eng.: A 765 (2019), https://doi.org/10.1016/j.msea.2019.138276.
[16] B.B. He, S. Pan, Correlation between martensitic transformation and strain burst in retained austenite grains during nanoindentation investigation, Met. Mater. Int. 28 (2022) 573–578, https://doi.org/10.1007/s12540-020-00913-4.
[17] S. Zhou, F. Hu, K. Wang, C. Hu, W. Zhou, S. Yershov, K. Wu, Z. Zhang, X. Pan, Nanomechanics of retained austenite in medium-carbon low-temperature bainitic steel: a critical analysis of a one-step versus a two-step treatment, Materials 15 (2022), https://doi.org/10.3390/ma15175996.
[18] L. Morales-Rivas, A. González-Orive, C. Garcia-Mateo, A. Hernández-Creus, F. G. Caballero, L. Vázquez, Nanomechanical characterization of nanostructured bainitic steel: peak force microscopy and nanoindentation with AFM, Sci. Rep. 5 (2015), https://doi.org/10.1038/srep17164.
[19] R. Lehnert, A. Weidner, M. Motylenko, H. Biermann, Strain hardening of phases in high-alloy CrMnNi steel as a consequence of pre-deformation studied by nanoindentation, Adv. Eng. Mater. 21 (2019), https://doi.org/10.1002/adem.201800801.
[20] T.H. Ahn, C.S. Oh, D.H. Kim, K.H. Oh, H. Bei, E.P. George, H.N. Han, Investigation of strain-induced martensitic transformation in metastable austenite using nanoindentation, Scr. Mater. 63 (2010) 540–543, https://doi.org/10.1016/j.scriptamat.2010.05.024.
[21] F.J. Ulm, M. Vandamme, H.M. Jennings, J. Vanzo, M. Bentivegna, K.J. Krakowiak, G. Constantinides, C.P. Bobko, K.J. Van Vliet, Does microstructure matter for statistical nanoindentation techniques? Cem. Concr. Compos 32 (2010) 92–99, https://doi.org/10.1016/j.cemconcomp.2009.08.007.
[22] T.H. Pham, S.E. Kim, Nanoindentation for investigation of microstructural compositions in SM490 steel weld zone, J. Constr. Steel Res 110 (2015) 40–47, https://doi.org/10.1016/j.jcsr.2015.02.020.
[23] E. Rossi, J.M. Wheeler, M. Sebastiani, High-speed nanoindentation mapping: a review of recent advances and applications, Curr. Opin. Solid State Mater. Sci. 27 (2023), https://doi.org/10.1016/j.cossms.2023.101107.
[24] H. Besharatloo, J.M. Wheeler, Influence of indentation size and spacing on statistical phase analysis via high-speed nanoindentation mapping of metal alloys, J. Mater. Res 36 (2021) 2198–2212, https://doi.org/10.1557/s43578-021-00214-5.
[25] S. Janakiram, P.S. Phani, G. Ummethala, S.K. Malladi, J. Gautam, L.A.I. Kestens, New insights on recovery and early recrystallization of ferrite-pearlite banded cold rolled high strength steels by high speed nanoindentation mapping, Scr. Mater. 194 (2021), https://doi.org/10.1016/j.scriptamat.2020.113676.
[26] G. Cheng, K.S. Choi, X. Hu, X. Sun, Application of nano-indentation test in estimating constituent phase properties for microstructure-based modeling of multiphase steels, SAE Int J. Engines 10 (2017) 405–412, https://doi.org/10.4271/2017-01-0372.
[27] S. Bhowmick, M.M. Nowell, 2016, , Mech. Prop. Ferrite Austenite Phases Duplex Steel.: A Comb. EBSD SEM Nanoindentation Study..
[28] T. Zhang, H. Xie, M. Huo, F. Jia, L. Li, D. Pan, H. Wu, J. Liu, T. Yang, F. Jiang, Z. Jiang, A method for the determination of individual phase properties in multiphase steels, Mater. Sci. Eng.: A 854 (2022), https://doi.org/10.1016/j.msea.2022.143707.

[29] Y. Chang, M. Lin, U. Hangen, S. Richter, C. Haase, W. Bleck, Revealing the relation between microstructural heterogeneities and local mechanical properties of complex-phase steel by correlative electron microscopy and nanoindentation characterization, Mater. Des. 203 (2021), https://doi.org/10.1016/j.matdes.2021.109620.
[30] Oxford Instruments, ⟨https://www.ebsd.com/ebsd-applications/what-information-does-ebsd-provide⟩, (2023).
[31] Oxford Instruments, ⟨https://www.ebsd.com/ebsd-explained/what-is-ebsd⟩, (2023).
[32] Oxford Instruments, ⟨https://www.ebsd.com/ois-ebsd-system/advanced-phase-discrimination⟩, (2023).
[33] Oxford Instruments, ⟨https://www.ebsd.com/ebsd-techniques/techniques-for-indexing⟩, (2023).
[34] Oxford Instruments, ⟨https://www.ebsd.com/ebsd-techniques/displaying-ebsd-data⟩, (2023).
[35] Oxford Instruments, ⟨https://www.ebsd.com/ebsd-explained/basics-of-automated-indexing⟩, (2023).
[36] E.S. Puchi-Cabrera, E. Rossi, G. Sansonetti, M. Sebastiani, E. Bemporad, Machine learning aided nanoindentation: a review of the current state and future perspectives, Curr. Opin. Solid State Mater. Sci. 27 (2023), https://doi.org/10.1016/j.cossms.2023.101091.
[37] ASTM, ⟨www.astm.org/e0415-21.html⟩, (2021).
[38] Oxford Instruments, ⟨https://www.ebsd.com/hints-and-tips/ebsd-sample-preparation⟩, (2023).
[39] P. Sudharshan Phani, W.C. Oliver, A critical assessment of the effect of indentation spacing on the measurement of hardness and modulus using instrumented indentation testing, Mater. Des. 164 (2019), https://doi.org/10.1016/j.matdes.2018.107563.
[40] M. Nowell, S. Wright, J. Carpenter, Differentiating Ferrite and Martensite in Steel Microstructures Using Electron Backscatter Diffraction, 2009. ⟨https://www.researchgate.net/publication/267777956⟩.
[41] C.J. Chiang, S. Bull, C. Winscom, A. Monkman, A nano-indentation study of the reduced elastic modulus of Alq3 and NPB thin-film used in OLED devices, Org. Electron 11 (2010) 450–455, https://doi.org/10.1016/j.orgel.2009.11.026.
[42] S. Zhou, F. Hu, K. Wang, C. Hu, H. Dong, X. Wan, S. Cheng, R.D.K. Misra, K. Wu, A study of deformation behavior and stability of retained austenite in carbide-free bainitic steel during nanoindentation process, J. Mater. Res. Technol. 20 (2022) 2221–2234, https://doi.org/10.1016/j.jmrt.2022.08.016.
[43] Y. Chang, C. Haase, D. Szeliga, L. Madej, U. Hangen, M. Pietrzyk, W. Bleck, Compositional heterogeneity in multiphase steels: characterization and influence on local properties, Mater. Sci. Eng.: A 827 (2021), https://doi.org/10.1016/j.msea.2021.142078.
[44] Q. Jia, H. Zhang, Y. Wang, S. Liu, S. Hao, L. Chen, X. Ma, Z. Zou, M. Jin, Assessment of stress partitioning of a TWIP + TRIP aided lean duplex stainless steel based on the nanoindentation and its application on the twinning evolution, Mater. Charact. 179 (2021), https://doi.org/10.1016/j.matchar.2021.111367.
[45] Q. Furnémont, M. Kempf, P.J. Jacques, M. Gö Ken, F. Delannay, On the measurement of the nanohardness of the constitutive phases of TRIP-assisted multiphase steels, 2002. ⟨www.elsevier.com/locate/msea⟩.
[46] P.J. Jacques, Q. Furnémont, F. Lani, T. Pardoen, F. Delannay, Multiscale mechanics of TRIP-assisted multiphase steels: I. Characterization and mechanical testing, Acta Mater. 55 (2007) 3681–3693, https://doi.org/10.1016/j.actamat.2007.02.029.
[47] J. Kang, N.S. Pottore, H. Zhu, C.C. Tasan, An in situ investigation of neighborhood effects in a ferrite-containing quenching and partitioning steel: Mechanical stability, strain partitioning, and damage, Acta Mater. 254 (2023), https://doi.org/10.1016/j.actamat.2023.118985.
[48] Y. Zhang, C. Wang, K.M. Reddy, W. Li, X. Wang, Study on the deformation mechanism of a high-nitrogen duplex stainless steel with excellent mechanical properties originated from bimodal grain design, Acta Mater. 226 (2022), https://doi.org/10.1016/j.actamat.2022.117670.
[49] X.K. Shang, S. Pan, Q.W. Guan, B.B. He, Orientation dependent twinning behavior in a twinning-induced plasticity steel investigated by nanoindentation, Met. Mater. Int. 28 (2022) 2874–2883, https://doi.org/10.1007/s12540-022-01180-1.
[50] S. Kang, Y.S. Jung, B.G. Yoo, J. il Jang, Y.K. Lee, Orientation-dependent indentation modulus and yielding in a high Mn twinning-induced plasticity steel, Mater. Sci. Eng. A 532 (2012) 500–504, https://doi.org/10.1016/j.msea.2011.10.116.
[51] R.A. Rijkenberg, M.P. Aarnts, F.A. Twisk, M.J. Zuijderwijk, M. Knieps, H. Pfaff, Linking crystallographic, chemical and nano-mechanical properties of phase constituents in DP and TRIP steels, in: Materials Science Forum, Trans Tech Publications Ltd, 2010, pp. 3465–3472, https://doi.org/10.4028/www.scientific.net/MSF.638-642.3465.
[52] S. Lu, B. Zhang, X. Li, J. Zhao, M. Zaiser, H. Fan, X. Zhang, Grain boundary effect on nanoindentation: a multiscale discrete dislocation dynamics model, J. Mech. Phys. Solids 126 (2019) 117–135, https://doi.org/10.1016/j.jmps.2019.02.003.
[53] J. Zhang, S. Zaefferer, Influence of sample preparation on nanoindentation results of twinning-induced plasticity steel, Int. J. Miner., Metall. Mater. 28 (2021) 877–887, https://doi.org/10.1007/s12613-021-2260-z.
[54] F. Bignoli, S. Rashid, E. Rossi, S. Jaddi, P. Djemia, G. Terraneo, A. Li Bassi, H. Idrissi, T. Pardoen, M. Sebastiani, M. Ghidelli, Effect of annealing on mechanical properties and thermal stability of ZrCu/O nanocomposite amorphous films synthetized by pulsed laser deposition, Mater. Des. 221 (2022), https://doi.org/10.1016/j.matdes.2022.110972.
[55] E.P. Koumoulos, K. Paraskevoudis, C.A. Charitidis, Constituents phase reconstruction through applied machine learning in nanoindentation mapping data of mortar surface, J. Compos. Sci. 3 (2019), https://doi.org/10.3390/jcs3030063.